T. Craciunescu, A. Murari, I. Tiseanu, J. Vega
and JET EFDA contributors

Supervised Image Processing Learning for Wall MARFE Detection Prior to Disruption in JET with a Carbon Wall

Supervised Image Processing Learning for Wall MARFE Detection Prior to Disruption in JET with a Carbon Wall

T. Craciunescu[1], A. Murari[2], I. Tiseanu[1], J. Vega[3]
and JET EFDA contributors*

JET-EFDA, Culham Science Centre, OX14 3DB, Abingdon, UK

[1]*EURATOM-MEdC Association, NILPRP, Bucharest, Romania*
[2] *Consorzio RFX, Associazione EURATOM-ENEA per la Fusione, Padova, Italy*
[3]*Asociación EURATOM/CIEMAT para Fusión, Madrid, Spain*
* See annex of F. Romanelli et al, "Overview of JET Results",
(24th IAEA Fusion Energy Conference, San Diego, USA (2012)).

ABSTRACT

In the last years several diagnostic systems have been installed on JET providing new information which may be potentially useful also for disruption prediction. The fast visible camera can deliver information about the occurrence of MARFE (Multifaceted Asymmetric Radiation From the Edge) instabilities which precede disruptions in density limit discharges. Two image processing methods – the Sparse Image Representation (SIR) using overcomplete dictionaries and the Histogram of Oriented Gradients (HOG) – have been used for developing MARFE classifiers with supervised learning. The methods have been tested with JET experimental data and a good prediction rate has been obtained. The HOG method is able to provide predictions useful for online disruption prediction.

INTRODUCTION

Disruptions represent a key issue for the operation of the next generation of tokamaks and in particular for ITER. The sudden loss of confinement may lead to very harmful events. During a short time interval, a large heat load can be deposited on the first wall. A following plasma current quench induces eddy currents on the surrounding metallic structures, leading to high electromagnetic forces [1-2]. The vertical stability of the plasma can also be compromised, particularly in the case of elongated plasmas which are more vertically unstable. The following vertical displacement events (VDE) usually cause the highest forces. The fast current quench may lead also to the production of relativistic runaway electrons [3] which can cause significant damages to the plasma facing components and to the first wall. Disruptions may lead also to deconditioning and therefore long periods of time may be necessary for recovering the optimal operational conditions.

The risk associated with disruptions is already quite significant for the present large devices. The disruption rate can be reduced but not completely avoided. In JET, with the carbon wall, the rate was reduced to 3.4% [4] while with the new full-metal ITER-like wall (ILW) this rate increased to 8% [5]. For ITER the risk is significantly higher due to the much higher plasma energy content. The engineering limit for the ITER disruption rate is about 10%, with 1% cases for those in which VDE are developed [6].

Therefore a significant effort has been dedicated during the last years to the understanding of the disruption causes and to the development of prediction and mitigation methods in order to minimise the structural damages and the erosion of plasma facing components.

The main factors triggering disruptions are believed to be, as summarized in [7], the following: i) Mode Lock (ML), ii) Density Limit (DL), iii) High Radiated Power (RP), iv) d) H/L mode transition (HL), v) Internal Transport Barrier (IT), vi) Vertical Displacement Event (VDE). However, as proved in Ref. 4, the root causes for the majority of disruptions are related with various instabilities and/ or failures of the control systems. A surveying picture of the causes generating disruptions in JET [5] showed that they are structured in highly complex patterns of chain events.

Automatic machine learning techniques have proved to be able to tackle with this complexity. These methods extract the useful information from complex combinations of several measured plasma diagnostic parameters related to several destabilizing factors. In these approaches the

disruptions are considered to be triggered by an initiating event with subsequent precursors which can be identified in plasma diagnostic signals. The predictor is then constructed based on detecting disruption precursors with suitable online diagnostics. The learning from examples mechanism succeeds to overcome the difficulties which arise from the non-linear nature of disruptions and from the influence of the electromagnetic properties of the devices, which is believed to play a significant role in the evolution of the disruptions.

The first approaches were based on artificial neural networks [8-10] . They succeeded to provide a high prediction rate, but the time interval between the prediction and the moment when the disruption occurs was of the order of a few milliseconds. Earlier predictions (several hundreds of milliseconds before the disruption) were provided later by approaches based on fuzzy logic techniques (see e.g. Refs. 11-14). Successful approaches dedicated to JET disruption prediction were also reported [15-16]. Recently a new predictor, called the Advanced Predictor Of DISruptions (APODIS), [17] was developed at JET. APODIS is a combination of supervised classification systems, based on a support vector machines (SVMs). It was deployed in real-time during the last campaigns with the ILW providing very good results: detection of 300 out of 305 disruptions and a very low number of false alarms [18]. The very early prediction allows the use of various mitigation tools for reducing the detrimental effects of the disruptions on the plasma facing components and vacuum vessel. The automatic classification of the disruptions type represents also a very important issue in order to allow the optimal choice for the mitigation strategy. An approach based on clustering using the geodesic distance was recently reported [19]. It is able to take into account the error bars of the measurements uncertainties, leading to a more precise classification. The method is suitable for online implementation.

In the last years several diagnostic systems have been installed in JET providing new information which may be potentially useful also for disruption prediction. For example, both infrared [20] and fast visible [21] cameras, installed on the wide angle endoscope [22], can provide information about the occurrence of MARFE (Multifaceted Asymmetric Radiation From the Edge) instabilities [23-25] which normally precede density limit. MARFEs cause a significant increase in impurity radiation, and therefore, they leave a clear signature in the video data. This footprint, which occur several hundreds of milliseconds before the disruption, can be used for automatic early identification.

On JET several methods were developed in the last years for MARFE identification and tracking. Different principles like morphological operators and HU moments [26] and phase congruency [27] and also a tracking method, based on the motion estimation within the MPEG video compressed domain [28], proved to work successfully. Currently, on JET, the fast imaging systems are not yet used for their real-time control because real time data streaming is not yet available. However valuable approaches were already proposed for real-time identification of MARFEs. A first attempt was based on the real-time image processing capability of cellular nonlinear neural network–based chips [29]. Recently, a highly parallelized implementation of the method introduced in Ref. 30 achieved an image processing rate of more than 10 000 frame per second.

The present approach investigates the MARFE identification potential of two image processing

2

methods, based on supervised learning strategies, which achieved significant results in computer vision and surveillance: Sparse Image Representation (SIR) [31] and Histogram of Oriented Gradients (HOG) [32]. SIR leaded, in the last years, to significantly improved results especially for image denoising [33] and encouraging results were reported also for texture segmentation [32] and object recognition [35-36]. HOG proved to significantly outperform existing methods for human detection by analysing the video sequences provided by visible and infra-red cameras (see e.g. Refs. 37-38). Significant results were reported also for face and gesture recognition (see e.g. Refs. 39-40), and vehicle detection [41].

With regard to the structure of the paper, the next section provide a briefly description of the SIR and HOG methods. Section 3 reports in detail the implementation of these methods for MARFE automatic identification in JET videos. The performances of the methods and the suitability for on-line implementation are also discussed this section. Several conclusions are drawn in the last section of the paper.

2. METHODS

2.1 SPARSE IMAGE REPRESENTATION

The sparse image representation consists of representing signals using an overcomplete dictionary that contains prototype image-atoms. The signal is represented as a linear combination of the image-atoms. The optimal overcomplete dictionary ensures the lowest reconstruction error, given a fixed sparsity factor L (number of coefficients in the representation). Arranging the atoms along the columns of the dictionary matrix $D \in R^{N \times K}$ is the total number of pixels in the image and is the total number of atoms in the dictionary), the representation of the image f can be formulated using the relation:

$$f \approx D\alpha$$
$$such\ that\ \|g\|_0 \leq S \tag{1}$$

where α is a sparse vector of approximation coefficients, the l_0 norm $\| \ \|_0$ counts the number of non-zero coefficients and S is the number of active atoms in the representation. The dictionary can be a fixed, general one (DCT, wavelet, curvelets, etc) but it was proved that improved results are obtained by learning non-parametric dictionaries simultaneously with the signal representation (see e.g. Ref. 29).

Thus, the reconstructive dictionary D is learned adaptively from the data such that the respective decomposition is sparse (i.e., no more than L non-zero elements), by solving the optimization problem:

$$\{\alpha, D, f\} = argmin_{\alpha,D,g}\left\{ \underbrace{\sum_{j=1}^{M}\|g_j - D\alpha_j\|_2}_{\substack{image \\ reconstruction}} + \lambda \underbrace{\sum_{l=1}^{L}\|\alpha_l\|_0}_{sparsity} \right\} \tag{2}$$

where λ is a regularisation parameter. Since images are usually large, the decomposition is implemented on overlapping image patches $g_j = P_j f$ instead of the whole image f (P_j is the operator

which extracts a specific patch g_j from the image f; M is the total number of patches). The first term of the objective function quantifies the signal reconstruction error while the second one measures the representation sparsity.

The usual strategy is based on iterative algorithms which start with an initial guess of D and alternates between sparse coding (finding the matrix of sparse approximation coefficients given a fixed dictionary) and dictionary update (adjusting the dictionary D given a fixed approximation coefficient matrix). In the first step the orthogonal matching pursuit (OMP) algorithm [42] is an efficient tool to decompose the image signals with respect to the given dictionary. In the second step a least-squares problem is solved for updating all the atoms simultaneously. The K-SVD algorithm [43], generalizing the K-means clustering process, succeed to obtain significant acceleration by combining, in the second step, the update of the dictionary columns with an update of the sparse representations. After the training process the atoms are adapted to the training set of images.

The image classification can be obtained by learning multiple dictionaries (one dictionary for each class of images) which are simultaneously reconstructive and discriminative. In principle a signal belonging to one class is reconstructed poorly by a dictionary corresponding to another class. The classification can be performed by using residual reconstruction errors of a signal by the dictionary belonging to a class as a discriminative operator for classification.

The discriminative power of the dictionaries is related to their mutual incoherency. Incoherent dictionaries are desirable whenever sparse approximations are used for revealing a certain underlying structure or clustering in the data. The coherence of a dictionary indicates the degree of similarity between different atoms. A measure of the mutual coherence is defined as the maximum absolute inner product between any two different atoms of the dictionary:

$$\mu(D) = max_{i \neq j} |\langle d_i, d_j \rangle|_2 \tag{3}$$

where d_i are the elements of the dictionary D.

If multiple dictionary are used (a dictionary for each class for example) then mutual incoherence between them have to be also promoted. A discriminative term can be introduced in (2) in order to encourage dictionaries associated to different classes to be as independent as possible, while still allowing for different classes to share features [44]:

$$\{\alpha, D, f\} = argmin_{\alpha, D, g} \left\{ \underbrace{\sum_{j=1}^{M} \|g_j - D\alpha_j\|_2}_{\substack{image \\ reconstruction}} + \lambda \underbrace{\sum_{l=1}^{L} \|\alpha_l\|_0}_{sparsity} \right\} + \eta \sum_{i \neq j} \|D_i^T D_j\|_F^2 \tag{4}$$

where the dictionary incoherence term is calculated using the Frobenius norm [45].

However, atoms representing common features in all classes tend to appear in all dictionaries. The corresponding reconstruction coefficients have a high absolute value. This lead to similar reconstruction errors for different dictionaries and does not allow a sharp classification. The

4

discrimination power can be increased by ignoring the coefficients associated to these common atoms when computing the reconstruction error. These atoms may be identified by inspecting the already available inner products between atoms $D_i^T D_j$. A certain threshold can be used to select the most discriminative atoms. In a recent approach [44], a de-correlation step is introduced in the dictionary update step. The decorelation is accomplished by an iterative projection method complemented by a rotation of the dictionary.

2.2 THE HISTOGRAM OF ORIENTED GRADIENTS

The use of edge orientation histogram in object recognition became very popular together with the introduction of SIFT (*Scale Invariant Feature Transform*) descriptors [47-48].

The SIFT key-points are extracted at the local extrema of the scale-space representation of the image, ensuring in this way invariance to scale change. The key-points are then represented using histogram of gradients. A dominant direction is determined and it is used as a reference for all image gradients. As the gradient structure is very characteristic of local shape, SIFT proved to be very effective in extracting distinctive features from images which are used for matching of different views of a scene.

The Histogram of Oriented Gradients (HOG) descriptors can be viewed as inherited from the SIFT descriptors. The basic idea, formulated by Dalal and Triggs [32], is that the local object shape can be well approximated by the distribution of edge directions, even without precise knowledge of the corresponding gradient or edge positions. In contrast with SIFT descriptors, which are computed at a sparse set of scale and rotation invariant key points, and used individually, HOG descriptors use a dense representation of the image by means of a local statistic of edge orientations. While SIFT descriptors are optimized for sparse matching, HOG descriptors rely on a dense robust coding of shapes.

The HOG descriptor is constructed as a pack of histograms. First the image is divided in a number of cells N_c with $N_x \times N_y$ pixels (Fig.1). After calculating the image gradient, the histogram of gradients is calculated for each cell, using N_0 bins. As proved in Ref.32 the most efficient way for calculating the image gradient is a simple one, by image filtering using the one-dimensional filter $(-1\ 0\ 1)$ and its transpose. Within a cell, every pixel votes for its gradient orientation weighted by its gradient magnitude. This procedure strengthens the votes of the pixels located on an edge in respect with those of the pixels located nearly uniform regions. Additionally the contribution of each pixel to the gradient histogram can be weighted by a Gaussian window and distributed into adjacent spatial cells and orientation bins using trilinear interpolation in order to avoid boundary effects [39]. Due to contrast changes in the image sequence cells histograms are locally normalized. Several cells are grouped in a block (see again Fig.1) and the normalisation is performed at the level of a block using *L1*-norm $V \to V / \sqrt{\|V\|_1 + \varepsilon}$ or *L2*-norm $V \to V / \sqrt{\|V\|_2^2 + \varepsilon^2}$ schemes – V is the unnormalised descriptor vector and is a regularising constant needed for example in case of zero gradients. Overlapping blocks allow a specific cell to be involved in different block normalisation operations. According Dalal and Triggs this redundancy may significantly improves the performances

of the HOG descriptor. Block normalisation can be followed by clipping, which limits the values of to a certain limit (typically 0.2) in order to reduce non-linear illumination changes. All histograms in a block are combined as a vector and all these vectors are concatenated in a single feature vector.

A detailed analysis of the influence of all the ingredients implied in the HOG descriptor calculation was performed in Ref. 32. Their main conclusion, derived from this analysis emphasizes outline that fine scale derivatives, many orientation bins and block-based normalisation are usually essential for good performance. Smoothing should be avoided because blurring may hide the foreground-to-contour transition which is critical for object identification. A coarse space quantisation, with its size adapted to the size of the objects to be identified in the image is sufficient for obtaining a good descriptor.

The HOG descriptors are usually associated with Support Vector Machines (SVM) classifiers [49]. SVM are based on the concept of decision planes that define decision boundaries. When data is not linearly separable, the kernel trick technique is applied. A function is used for mapping the input space into a higher dimensional linear separable feature space. For a training data set $\{x_k, y_k\}$, where x_k are the training examples HOG feature vector, and $y_k \in \{-1,1\}$ the known class labels, the algorithm search for the maximum-margin hyper-plane $f(x) = w \cdot f(x) + b$ that divides the points belonging to the two classes. This hyper-plane lies furthest from the data sets belonging to both classes. This can be imagined as two hyper-planes (the so called supporting planes) that start from the boundary and are pushed apart towards the points corresponding to the two classes:

$$\begin{cases} f(x) = 1, \text{ for the points with the class label } +1 \\ f(x) = -1, \text{ for the points with the class label } -1 \end{cases} \tag{5}$$

This relation can be rewritten as:

$$y_i f(x_i)) \geq 1 \tag{6}$$

The region bounded by them is called "the margin". The distance between the supporting planes is $2/\| w \|_2$. Maximising the distance is equivalent with minimizing the following problem:

$$min_{w,b} \frac{1}{2} \|w\|^2 \tag{7}$$

The maximisation is performed subject to condition (5) in order to prevent data points from falling into the margin. The vector w is known as the weight vector. The weights directly reflect the importance of a feature in discriminating the two classes.

However, usually noise or outliers may affect the data and influence the determination of the boundary. The soft margin technique [50] is used in order to make the classifier insensitive to noise in the data. It consists in relaxing the condition for the optimal hyper-plane by allowing a certain amount of slackness:

$$y_i(f(x_i)) \geq 1 - \xi_i, i = 1, ..., N \tag{8}$$

The introduction of slack variables ξ_i, which measure the degree of misclassification of the data , lead to an additional term in the minimisation problem:

$$min_{w,b} \frac{1}{2} \|w\|^2 + C_{w,b} \sum_{j=1}^{M} \|w\|^2 \tag{9}$$

The minimisation problem searches for the optimum compromise between a large margin and a small error penalty.

3. APPLICATION FOR MARFE IDENTIFICATION IN JET VIDEOS
3.1 VIDEO RECORDING OF MARFE INSTABILITIES AT JET
The MARFE instability is a tokamak edge phenomenon characterized by greatly increased radiation and density, by density fluctuations, and by decreased temperature in a relatively small volume. MARFEs usually occur on the high-field side of the torus and are the manifestation of a thermal instability, with impurity radiation being the main energy loss mechanism from its volume. The impurity radiation is the cause of the specific signature which appears in the videos recorded by the wide angle fast visible camera (Fig.2). The identification method must be able to avoid the confusion with other video objects, like e.g. flashes, probably caused by ELMs (Edge Localized Modes) or high radiation from the poloidal limiters (Fig.3).

The MARFE image database was described in Ref.30 and it is summarised in table 1. It contains videos recorded using the wide angle fast visible camera. The camera is viewing the full poloidal cross-section of the vacuum vessel and it is covering a toroidal extent of 90°. The wide angle view is designed for the study of pellet ablation, large scale instabilities and plasma wall interactions. It can grab an image at each ~33ms which impose a tough limit for on-line MARFE detection.

A learning data set has been built by selecting 50 images containing MARFEs in case of the SIR method. For the HOG method the training set includes also a distinct set containing 50 images containing objects with morphological characteristics similar to MARFE and 50 images displaying all other type of objects. After training the methods have been tested on the rest of the existing data.

3.2 SIR IMPLEMENTATION AND RESULTS
Several strategies were tested for using SIR as a MARFE detector, aiming at a high identification rate, a low number of false alarms and also at minimising the computation time. The best results have been obtained by learning a dictionary for the MARFE images and then using this dictionary for image classification. The reconstructive dictionary D^{MARFE} has been learned adaptively from the data using the procedure described above. The minimisation of Eq.2 starts with random patches as a first guess of the dictionary elements and it was performed using the MATLAB implementation of the K-SVD algorithm [51]. We have used a dictionary size $K = 256$ and patches with a size of 8×8 pixels. In this stage the algorithm allows an arbitrary number of atoms to represent each image,

until a specific representation error $Err = \sum_{j=1}^{M} \|g_j - D\alpha_j\|_2$ is reached (the sparsity condition is not yet enforced). The representation error is related to the estimated noise in the gray-level image, assumed to be white Gaussian: , where is the standard deviation of noise. In the experiments presented in this paper , and is estimated using the method described in Ref.52. This method uses a zero mean operator which is almost insensitive to the image structure and it is implemented by mean of the mask $\begin{pmatrix} 1 & -2 & 1 \\ -2 & 4 & -2 \\ 1 & -2 & 1 \end{pmatrix}$. The mask is derived starting from the idea that image structures like edges have strong second order differential components and therefore a noise estimator should be insensitive to the Laplacean of an image. Thus the operator is derived using the difference between two masks which both approximate the Laplacean of the image. The learned dictionary is presented in Fig.4.

Then, using D^{MARFE}, for each new image in the test set, its representation $\{\alpha_j\}$ with respect to the dictionary has been determined. The sparsity condition is now applied, limiting the number of terms in the representation to $N_{terms} = 10$. The representation is implemented by decomposing the image in 8×8 pixel size patches (2 pixels overlapping), instead of using the whole images. The representation is determined using the OMP algorithm. OMP first find the one atom that has the biggest inner product with the signal, and then subtract the contribution due to that atom, and repeat the process until the signal is satisfactorily decomposed.

A similarity map between the image and its representation can be calculated using the following relation [53]:

$$SIM = \frac{2lm^{ini} \cdot lm^{rep} + T}{(lm^{ini})^2 + (lm^{rep})^2 + T} \tag{10}$$

where lm^{ini} is the current analysed image in the test set, lm^{rep} is its representation using the dictionary D^{MARFE} and T is a positive constant introduced in order to ensure the stability of the calculation of SIM. The SIM map, which contains similarity values calculated in each image pixel, can be pooled into a single similarity score by a summation over the image:

$$SIM_{score} = \sum_i SIM_i \tag{11}$$

A representative result is illustrated in Fig.5 for JET Pulse No: 50053. Both the MARFE and non-MARFE events produce peaks, but with a different width. Therefore SIR transforms the 2D image recognition task in a 1D problem. A threshold of $Th = 6$ frames full width at half maximum of the peak height (FWHM) has been introduced order to select the MARFE events. This value has been used for analysing all the test dataset. For the available video database, 94.8% of the MARFE events are correctly classified. Among the misclassified events, a rate of 4.4% are false positive events (like peak 'E' in Fig.5) and 0.8% are false negatives.

Unfortunately due to the iterative OMP procedure used for retrieving the image representation, the method cannot attempt to satisfy the on-line requirements in terms of computational time. However SIR may represent a useful tool for off-line analysis of large databases.

8

3.3 HOG IMPLEMENTATION AND RESULTS

The dense small block descriptors used by the HOG method have an excellent discrimination power, but the processing time needed for calculating HOG descriptors represents a critical issue. However different strategies were proposed to deal with this problem. One option consists of the use of a cascade of rejecters strategy [37]. AdaBoost is used to choose which features to evaluate in each stage, where each feature corresponds to one block. A different approach, followed in this work, relies on the parallel implementation of the HOG algorithm using the GPGPU (General Purpose computation on Graphics Processing Units) technology [54-56]. GPGPU uses the graphic processing unit (GPU) as a coprocessor for scientific computations. The CUDA (*Compute Unified Device Architecture*) software platform provide a hardware abstraction mechanism which, hides the GPU hardware for the programmer and allows the translation of the C/C++ code onto the GPU for that part of the application code which supports a massive parallelization. Functions are executed in multiple (usually thousands) parallel threads. Multiple threads are grouped in CUDA-blocks and multiple CUDA-blocks are assembled in a grid. Threads have access to several types of memory (register, local, shared, global, constant and texture). All threads can access global memory but only threads in the same block can cooperate by using a shared memory and by synchronization. Global memory access is typically two orders of magnitudes slower than shared memory access. Therefore the access to the global memory represents usually the bottleneck of the CUDA implementations. The implementation of the HOG descriptors method for MARFE automatic identification has been performed by modifying the code provided in Ref. 55 and taking into account the multiple factors which should be considered for a possible online implementation. In JET, with a carbon wall, the time elapsed between the occurrence of a MARFE and the following disruption is of the order of several hundreds of microseconds. This relatively relaxed time constraint is strongly sharpened by the frame rate of the fast visible camera which imposes a time constraint of 33 µs for image analysis and MARFE identification.

Fortunately the characteristics of the images provided by the camera can be exploited in order reduce the computation time for the HOG algorithm. A region of interest ROI, with a reduced size of $N_x \times N_y = 112 \times 172$ pixels, can be defined to encompass the area where all the MARFEs in the JET database leave a signature (Fig.6). Restricting calculations to ROI will reduce the computation time for gradients and SVM evaluation. However, an image with reduced size does not necessary lead to a straightforward decrease of the computation time, due to the time consuming copy operation between global and local memory. Therefore, in order to reduce the effect of the latency of global memory access, a set of N_{comb} images have been grouped in a combined image which is copied into GPU memory and then processed by the GPU.

The HOG algorithm spends a significant part of the time for the block histogram computation (see again Ref. 51). Reducing the number of sliding windows may lead to a significant improvement in the computation speeds. The experiments that we have performed show that non-overlapping square HOG-blocks (one block coincides with one cell using the terminology introduced above) with a size of 16×16 pixels are sufficient for the discrimination of the MARFE shapes. This reduces

the histogram computation effort to a total number of 77 HOG-blocks for each image provided by the camera ($N_{comb} \times 77$ HOG-blocks for the combined image created by assembling the ROIs from consecutive images). The value must be large enough to avoid GPU latency but in the same time small enough to provide the MARFE detection result as fast as possible. $N_{comb} = 16$ represents a good compromise between these requirements.

Further improvement of the computation time can be obtained by taking into account that the fast visible camera provides grey-level images where MARFE and non-MARFE events (ELMs, UFOs etc.) appear mainly as bright features on a dark background and a low contrast variation appear along the image stream. Therefore the normalisation and clipping step can be omitted.

After implementing all these approximations, introduced for saving computation time, the algorithm have been extensively tested in order assess also the quality of the predictor. A representative result of this evaluation is reported in Fig.7, for the same JET pulse (Pulse No: 50053). An output value of 1, provided by the SVM, signals the occurrence of a MARFE event. The evolution of SVM output is represented together with the SIM index defined for the SIR method in order to allow a comparison of the response provided by the two methods. The HOG method provides a sharp answer for all the test dataset. The occurrence of MARFE events have been detected with a success rate of 100%, even if only 74.7% images displaying MARFE shapes have been identified. For the entire database, the classifier success rate remains at the level of 100% while 77.8% of MARFE frames are correctly identified. A reason for the difference between the identification rate for MARFE events and frames respectively is the use of the ROI. For all MARFE events, a certain number of frames, but not all of them, leave a signature inside the ROI. Also the selection of frames for building the training set may represent another reason for this difference.

As the prediction capability is very good, the algorithm, tailored as described above, has been implemented using a NIVIDIA Quadro 5000 GPU. The computation time for the SVM training is not a critical issue. Therefore this step was performed using the SPIDER [57], a complete object orientated environment for machine learning in MATLAB. After training the SVM weights have been stored for using them later as input for the code implemented on the GPU. The processing time needed for each ROI is 0.65ms. The computation time is approximately twenty times greater than the time interval between consecutive frames and obviously it does not allow the sequential analysis of all images in the video sequence. In order to tackle this problem it has been necessary to define a criterion to select the images susceptible to contain MARFE events and to restrict the analysis to this data subset. The criterion is based on the total brightness of the image. The sum S_g of the grey-level values for all pixels in each ROI is calculated for each image in the video stream and the HOG algorithm is launched only if S_g is above a certain threshold T_g. A typical example is presented in Fig.7. The red marks identify 17 intervals of interest (IOI), selected by using the threshold value $T_g = 0.1 \cdot S_g^{max}$, where S_g^{max} is the sum of grey-level values for the white image. This value of the threshold has been used for the analysis of all videos in the JET database. 10 intervals correspond to 8 MARFE events (in two cases the threshold is reached two times for the same event) and 10 intervals correspond to non-MARFE events. In one case (MARFE event M5), the gap between

the successive IOIs is lower than N_{comb} which means that immediately after the HOG analysis of a goup of images another one follow. A maximum sequence of 64 images should be analysed which means a total computation time of ~42ms. This is the maximum delay in signalling the MARFE occurrence. The average value of the time needed for prediction, calculated for the whole database, is 15.4ms. As the time difference between the MARFE occurrence and the following disruption is usually of the order of several hundreds of milliseconds, the HOG method is able to provide the prediction fast enough to allow time for mitigation tools in order to reduce the detrimental effects of disruptions.

CONCLUSION

Two MARFE classifiers with supervised learning have been developed. They are based on two image object identification methods. The first one uses sparse image representation of images using overcomplete dictionaries. A dictionary is retrieved for the MARFE class of images by training with an appropriate data set. Then the error of the representation of the images in the video sequences, using the determined dictionary, is used for classification. In the second method the HOG feature vectors are used as input for a SVM classifier. Both methods ensure a robust identification of MARFE events. It must be mentioned that the HOG method achieved 100% identification of MARFE events when applied to the JET database of discharges. Using a criterion based on threshold for the image total brightness for launching the calculations, the HOG method is able to provide the prediction fast enough to allow online disruption prediction. As mentioned in the introduction, effective online prediction will require also an upgrade of the hardware of the cameras since the ones presently used and with the right time resolution to identify MARFEs cannot perform real time streaming of the videos.

REFERENCES

[1] T.C. Hender, J.C Wesley, J. Bialek, A. Bondeson, A.H. Boozer, R.J. Buttery, A. Garofalo, T.P Goodman, R.S. Granetz, Y. Gribov, O. Gruber, M. Gryaznevich, G. Giruzzi, S. Günter, N. Hayashi, P. Helander, C.C. Hegna, D.F. Howell, D.A. Humphreys, G.T.A. Huysmans, A.W. Hyatt, A. Isayama, S.C. Jardin, Y. Kawano, A. Kellman, C. Kessel, H.R. Koslowski, R.J. La Haye, E. Lazzaro, Y.Q. Liu, V. Lukash, J. Manickam, S. Medvedev, V. Mertens, S.V. Mirnov, Y. Nakamura, G. Navratil, M. Okabayashi, T. Ozeki, R. Paccagnella, G. Pautasso, F. Porcelli, V.D. Pustovitov, V. Riccardo, M. Sato, O. Sauter, M.J. Schaffer, M. Shimada, P. Sonato, E.J. Strait, M. Sugihara, M. Takechi, A.D. Turnbull, E. Westerhof, D.G. Whyte, R. Yoshino, H.

Zohm, , MHD stability, operational limits and disruptions, Nuclear Fusion **47**(2007) S128.

[2] F.C.Schüller, Disruptions in tokamaks Plasma Physics and Controlled Fusion **37**(1995) A135–62.

[3] P. Helander, L.G. Eriksson, F Andersson, Runaway acceleration during magnetic reconnection in tokamaks, Plasma Physics and Controlled Fusion **44**(2002) B247

[4] P.C. de Vries, M.F. Johnson, B. Alper, P. Buratti, T.C. Hender, H.R. Koslowski, V. Riccardo, Survey of disruption causes at JET, Nuclear Fusion **51** -5(2011)053018.

[5] P C de Vries, G Arnoux, A Huber, J Flanagan, M Lehnen, V Riccardo, C Reux, S Jachmich, C Lowry, G Calabro, D Frigione, M Tsalas, N Hartmann, S Brezinsek, M Clever, D Douai, M Groth, T C Hender, E Hodille, E Joffrin, U Kruezi, G F Matthews, J Morris, R Neu, V Philipps, G Sergienko, M Sertoli, The impact of the ITER-like wall at JET on disruptions, Plasma Physics and Controlled Fusion **54**-12(2012) 124032.

[6] ITER load specification (ITER D 2MX47L) https://user.iter.org/?uid=2MX47L

[7] G. Pautasso, C. Tichmann, S. Egorov, T. Zehetbauer, O. Gruber, M. Maraschek, K.-F. Mast, V. Mertens, I. Perchermeier, G. Raupp, W. Treutterer, C.G. Windsor, On-line prediction and mitigation of disruptions in ASDEX Upgrade, Nuclear Fusion **42**-1(2002)100.

[8] J.V. Hernandez, A. Vannucci, T. Tajima, Z. Lin, W. Horton, S.C. McCool, Neural network prediction of some classes of tokamak disruptions, Nuclear Fusion **36**-8(1996)1009–17.

[9] Vannucci, K.A. Oliveira, T. Tajima, T., Forecast of TEXT plasma disruptions using soft x-rays as input signal in a neural network, Nuclear Fusion **39**-2(1999)255–62.

[10] A. Sengupta, P. Ranjan, Forecasting disruptions in the ADITYA tokamak using neural networks, Nuclear Fusion **40**-12(2000)1993–2008.

[11] G.Pautasso, C.Tichmann, S.Egorov, T.Zehetbauer, O.Gruber, M.Maraschek, K.F.Mast, V. Mertens, I.Perchermeier, G.Raupp, W.Treutterer, C.G.Windsor, ,On-line prediction and mitigation of disruptions in ASDEX Upgrade, Nuclear Fusion **42**-1(2002) 100–8.

[12] M.Versaci, F.C.Morabito, Fuzzy time series approach for disruption prediction in tokamak reactors, IEEE Transactions on Magnetics **39** 1503–6.

[13] B. Cannas, A. Fanni, E. Marongiu, P. Sonato, Disruption forecasting at JET using neural networks, Nuclear Fusion **44**-1(2004)68–76.

[14] G. Vagliasindi, A. Murari, P. Arena, L. Fortuna, M. Johnson, D. Howell, Fuzzy logic approach to disruption prediction at JET, IEEE Transactions on Plasma Sciences **36**-1(2008)253-262.

[15] B. Cannas, A. Fanni, P. Sonato, M.K. Zedda and JET-EFDA contributors Nuclear Fusion **47** No 11 (November 2007) 1559-1569

[16] B. Cannas, F. Cau, A. Fann, P. Sonato, M.K. Zedda, Nuclear Fusion **46**-7(2006)699-708.

[17] G.A. Ratta, J. Vega, A. Murari, G. Vagliasindi, M.F. Johnson, P.C. De Vries, An advanced disruption predictor for jet tested in a simulated real-time environment, Nuclear Fusion **50**(2010)025005.

12

[18] J. Vega, S. Dormido-Canto, J.M. López, A. Murari, J.M. Ramírez, R. Moreno, M. Ruiz, D. Alves, R. Felton, Results of the JET real-time disruption predictor in the ITER-like wall campaigns (2013) Fusion Engineering and Design, Article in Press, DOI: 10.1016/j.fusengdes.2013.03.00.

[19] A. Murari, P. Boutot, J. Vega, M. Gelfusa, R. Moreno, G. V erdoolaege, P.C. De Vries, Clustering based on the geodesic distance on Gaussian manifolds for the automatic classification of disruptions (2013) Nuclear Fusion, **53** (3), art. no. 033006.

[20] I.Balboa, G. Arnoux, T. Eich, B. Sieglin, S. Devaux, W. Zeidner, C. Morlock, U. Kruezi, G. Sergienko, D. Kinna, P.D. Thomas, M. Rack, Upgrade of the infrared camera diagnostics for the JET ITER-like wall divertor, Review of Scientific Instruments, 83-10(2012)10D530.

[21] J. A. Alonso, P. Andrew, A. Neto, J. L. de Pablos, E. de la Cal, H. Fernandes, J. Gafert, P. Heesterman, C. Hidalgo, G. Kocsis, A. Manzanares, A. Murari, G. Petravich, L. Rios, C. Silva, P.D. Thomas, Fast visible camera installation and operation in JET, International Conference on Burning Plasma Diagnostics, Varenna, Italy, 24–28 Sept. 2007, AIP Conf. Proc. 988, pp. 185-188.

[22] E. Gauthier, H. Roche, E. Thomas, S. Droineau, B. Bertrand, J.B. Migozzi, W. Vliegenthart, L. Dague, P. Andrew, T. Tiscornia, D. Sands, ITER-like wide-angle infrared thermography and visible observation diagnostic using reflective optics, Fusion Engineering and Design, **82-5–14**(2007) 1335-1340.

[23] H.B. Lipschultz, B. LaBombard, E.S. Marmar et al., "MARFE: An Edge Plasma Phenomenon", Nuclear Fusion, vol. **24**-8(1984) 977-988.

[24] M. Z. Tokar, J. Rapp, D. Reiser, U. Samm, F. C. Schuller, G. Sergienko and P. C. de Vries: Localized recycling as a trigger of MARFE, Journal of Nuclear Materials **266–269** (1999) 958

[25] J. Rapp, P.C. De Vries, F.C. Schüller, M.Z. Tokar, W. Biel, R. Jaspers, H.R. Koslowski, A. Krämer-Flecken, A. Kreter, M. Lehnen, A. Pospieszczyk, D. Reiser, U. Samm, and G. Sergienko, Density limits in TEXTOR-94 auxiliary heated discharges, Nuclear Fusion **39**, 765 (1999)

[26] Murari, A., Camplani, M., Cannas, B., Mazon, D., Delaunay, F., Usai, P., Delmond, J.F., Algorithms for the automatic identification of MARFEs and UFOs in JET database of visible camera videos, (2010) IEEE Transactions on Plasma Science, **38** (12 PART 2), art. no. 5599307, pp. 3409-3418.

[27] Craciunescu, T., Murari, A., Tiseanu, I., Vega, J., Phase congruency image classification for marfe detection on jet with a carbon wall (2012) Fusion Science and Technology, **62** (2), pp. 339-346.

[28] Craciunescu, T., Murari, A., Tiseanu, I., Lang, P. Motion estimation within the MPEG video compressed domain for JET plasma diagnostics, (2011) Nuclear Instruments and Methods in Physics Research, Section A: Accelerators, Spectrometers, Detectors and Associated

Equipment, **659** (1), pp. 467-476.

[29] G. Vagliasindi, A. Murari, P. Arena, L. Fortuna, G. Mazzitelli, Cellular Neural Network Algorithms for Real-Time Image Analysis in Plasma Fusion, Instrumentation and Measurement, IEEE Transactions on Volume: **58**-8(2009)2417 – 2425.

[30] M. Portes de Albuquerque, A. Murari, M. Giovani, N. Alves Jr., Marcelo P. de Albuquerque, A 10,000 images per second parallel algorithm for real time detection of MARFEs on JET, IEEE Transactions on Plasma Science, **41**-2(2013)341-349.

[31] M. Elad, Sparse and Redundant Representations: From Theory to Applications in Signal and Image Processing, Springer, 2010.

[32] N. Dalal, B. Triggs, Histograms of Oriented Gradients for Human Detection, International Conference on Computer Vision & Pattern Recognition (CVPR '05) 1 (2005) 886-893.

[33] M. Elad, M. Aharon, Image Denoising Via Sparse and Redundant Representations Over Learned Dictionaries, IEEE Transactions on Image Processing, **15**-12(2006)3736-3745.

[34] J. Mairal, F, Bach, J. Ponce, G. Sapiro, A. Zisserman, Discriminative learned dictionaries for local image analysis, Proc. of the IEEE Conference on Computer Vision and Pattern Recognition, 23-28 June 2008, Anchorage, USA, pp. 1-8.

[35] R. Sivalingam, G. Somasundaram, V. Morellas, N. Papanikolopoulos, O. Lotfallah, Y. Park, Dictionary Learning Based Object Detection and Counting in Traffic Scenes, Proceedings of the 4th ACM/IEEE International Conference on Distributed Smart Cameras (ICDSC), 2010.

[36] Q, Zhang, B. Li, Discriminative K-SVD for Dictionary Learning in Face Recognition, IEEE Conference on Computer Vision and Pattern Recognition (CVPR), IEEE Conference on Computer Vision and Pattern Recognition (CVPR), 13-18 June 2010, San Francisco, CA , pp. 2691 – 2698

[37] Q. Zhu, M.C. Yeh, K.T. Cheng ; S. Avidan, Fast Human Detection Using a Cascade of Histograms of Oriented Gradients, IEEE Computer Society Conference on Computer Vision and Pattern Recognition (CVPR) 17-22 June 2006, New York, NY, USA, p. 1491 – 1498.

[38] F. Suard, A. Rakotomamonjy, A. Bensrhair, A. Broggi, Pedestrian Detection using Infrared images and Histograms of Oriented Gradients, Proc. of Intelligent Vehicles Symposium 2006, June 13-15, 2006, Tokyo, Japan, p. 206-212.

[39] A. Albiol, D. Monzo, A. Martin, J. Sastre, A. Albiol, Face recognition using HOG-EBGM, Pattern Recognition Letters 29(2008)1537-1543.

[40] O. Déniz, G. Bueno, J. Salido, F. De la Torre, Face recognition using Histograms of Oriented Gradients, Pattern Recognition Letters **32** (2011) 1598–1603.

[41] X. Cao, C. Wu, P. Yan, X. Li, Linear SVM Classification Using Boosting HOG Features for Vehicle Detection in Low-Altitude Airborne Videos, 2011 18th IEEE International Conference on Image Processing (ICIP 2011), 11 Sep - 14 Sep 2011, Brussels, Belgium, p.2469-2472.

[42] G. Davis, S. Mallat, and M. Avellaneda, Adaptive greedy approximations, Journal Constructing Approximate, vol. **13**, pp. 57–98, 1997.

[43] M. Aharon, M., Elad, A., Bruckstein, K-SVD: An algorithm for designing overcomplete dictionaries for sparse representation, IEEE Transactions on Signal Processing, **54**-11(2006) 4311-4322.

[44] I. Ramirez, P. Sprechmann, G. Sapiro, Classification and Clustering via Dictionary Learning with Structured Incoherence and Shared Features, IEEE Conference on Computer Vision and Pattern Recognition (CVPR), 13-18 June 2010, San Francisco, CA , pp. 3501 – 3508

[45] G.H. Golub, C.F. Van Loan, Matrix Computations, 3rd ed. Baltimore, MD: Johns Hopkins, 1996.

[46] D. Barchiesi, M.D. Plumbley, Learning incoherent dictionaries for sparse approximation using iterative projections and rotations, IEEE Transactions on Signal Processing, **61**-8(2013) 2055-2065.

[47] D. G. Lowe, Distinctive image features from scale-invariant keypoints. IJCV, 60(2):91–110, 2004.

[48] K. Mikolajczyk and C. Schmid, A performance evaluation of local descriptors. PAMI, 27-10(2005)1615-1630.

[49] V.N. Vapnik, The Nature of Statistical Learning Theory, Springer-Verlag, 1995.

[50] C. Cortes, V. Vapnik, Support-vector networks, Machine Learning, 20-3(1995)273-297.

[51] M. Elad, M. Aharon, F. Bruckstein, K-SVD MATLAB Package, http://www.cs.technion. ac.il/~elad/software/.

[52] J. Immerkær, Fast Noise Variance Estimation, Computer Vision and Image Understanding, 64-2(1996)300-302.

[53] Z. Wang, A. C. Bovik, H. R. Sheikh, And E. P. Simoncelli, Image quality assessment: From error visibility to structural similarity, IEEE Trans. Image Process., **13**-4(2004)600–612.

[54] C. Wojek, G. Dorko, A. Schulz, B. Schiele, Sliding-windows for rapid object class localization: A parallel technique, Proc. of the 30th DAGM symposium on Pattern Recognition, pages 71–81, Berlin, Heidelberg, 2008, Springer-Verlag.

[55] V.A. Prisacariu, I.D. Reid, fastHOG - a real-time GPU implementation of HOG, http:// www.robots.ox.ac.uk/~lav/Papers/prisacariu_reid_tr2310_09/prisacariu_reid_tr2310_09. html, 2009.

[56] Y.P. Chen, S.Z. Li, X.M. LIN, Fast HOF Feature Computation based on CUDA, 2011 IEEE International Conference on Computer Science and Automation Engineering (CSAE), 1-12 June 2011, Shanghai, China, p. 748-751.

[57] J. Weston, A. Elisseeff, G. Bakir, F. Sinz, T. Joachims, C.-C. Chang, C.J. Lin, R. Collobert, J. Hill, J. Eichhorn, R. Fernandez, H. Froelich, G. Jemwa, K. Yang, C. Patel, S. Rojas, SPIDER - A complete object orientated environment for machine learning in Matlab, http://people. kyb.tuebingen.mpg.de/spider/main.html

No of videos	22
Total number of frames containing clear events	*4236*
Frames showing MARFEs	*16.9%*
Frames containing patterns with morphological characteristics similar to MARFE	*3.4%*
Frames showing Non-MARFE events	*79.7%*

Table 1: Characteristics of the MARFE video database at JET. All the videos were collected during operation with the carbon wall.
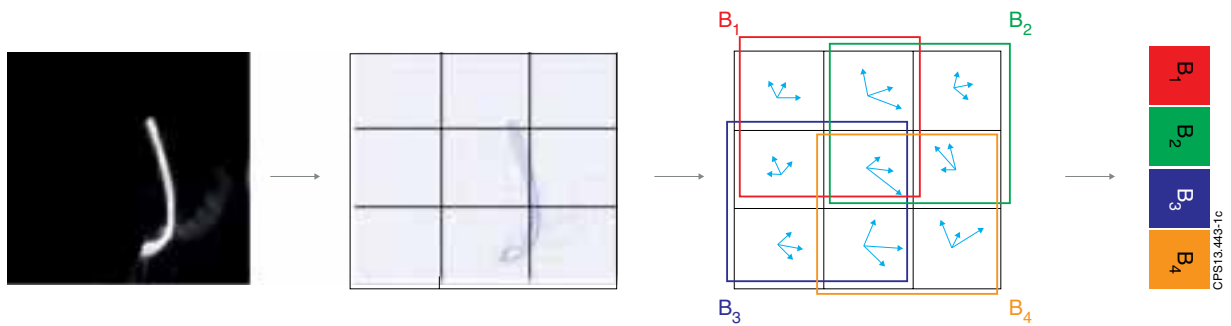

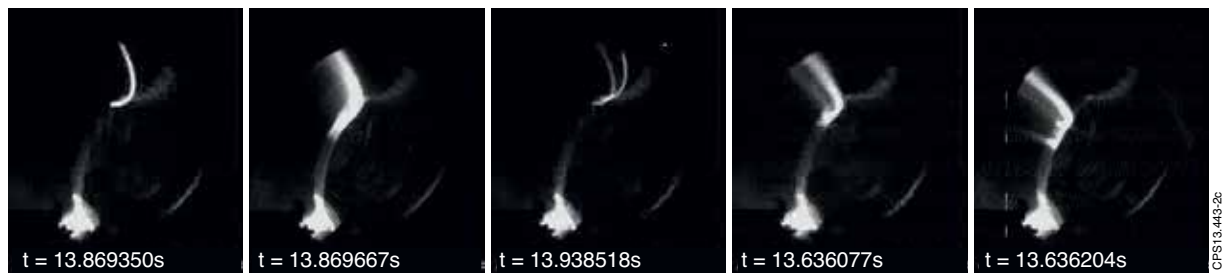
Figure 1: Illustration of the HOG descriptor calculation.

JET Pulse No: 70050

t = 13.869350s   t = 13.869667s   t = 13.938518s   t = 13.636077s   t = 13.636204s

Figure 2: Typical MARFE signatures on the JET videos.

JET Pulse No: 70050

t = 13.446927s   t = 13.387353s
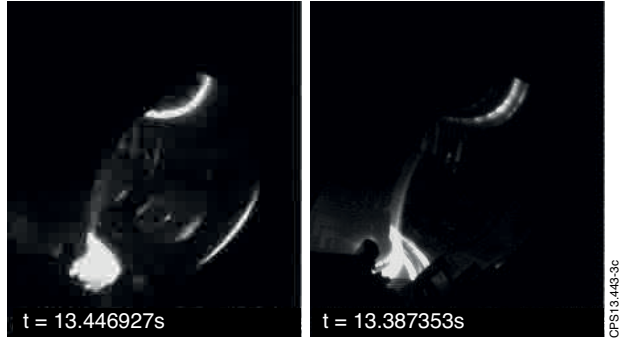
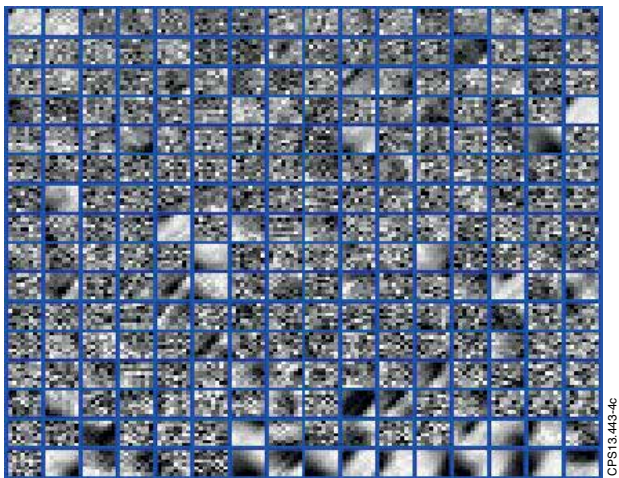*Figure 3: Frame showing shapes similar to MARFEs.*

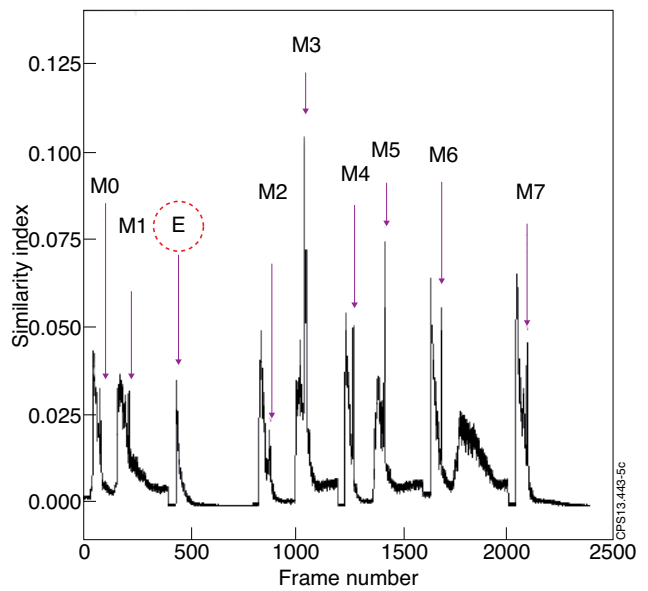*Figure 4: The dictionary retrieved using the MARFE learning dataset.*

Figure 5: The evolution of the SIM index for JET Pulse No: 50053. The MARFE events correctly identified are marked as M_i; E stands for an event incorrectly classified as a MARFE one.
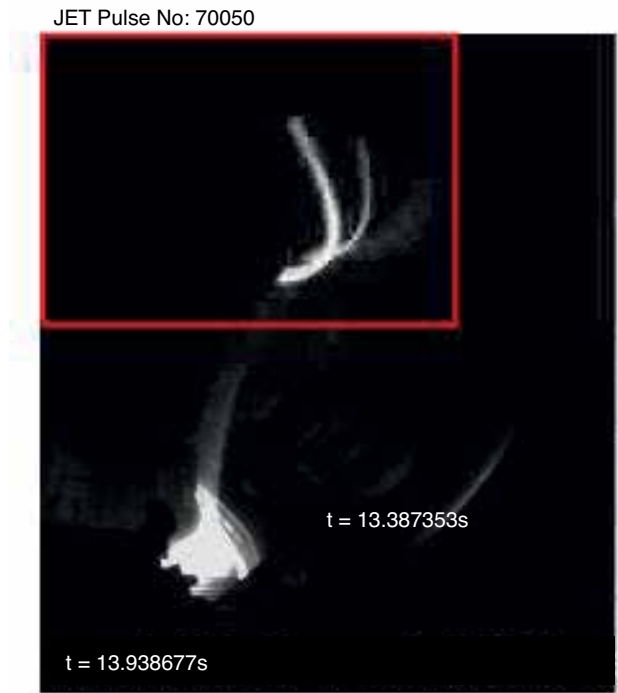
17

Figure 6: The region of interest defined for HOG computation.
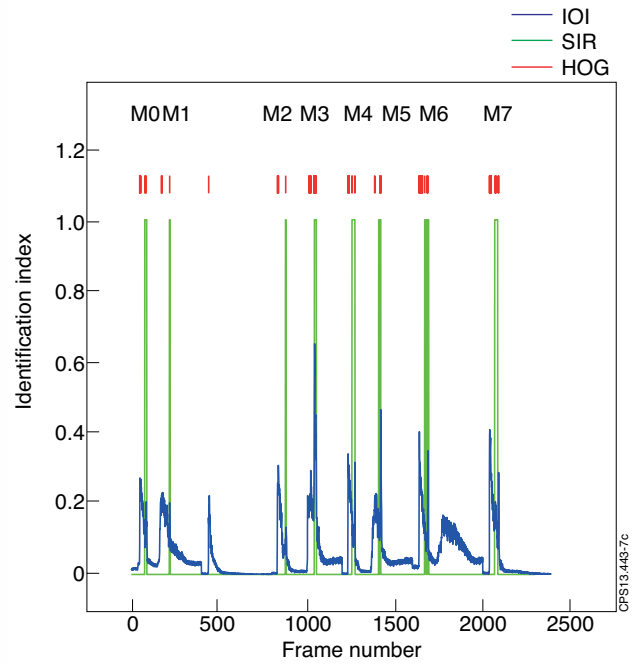

Figure 7: The evolution of the SVM output (green curve) signals the MARFE occurrence. The SIM index (Fig.5) is presented also in order to allow a comparison of the response provided by the two methods. The frames for which the HOG algorithm is launched are indicated by the red marks

18